NASA-CR-199320

FINAL
IN-89-CR
65720
P-35

A Study of Cooling Flows in Poor Clusters of Galaxies

Gerard A. Kriss

and

Stephen Dillingham
Department of Physics & Astronomy, Johns Hopkins University, Baltimore, MD 21218

Abstract

We observed three poor clusters with central dominant galaxies (AWM 4, MKW 4, and MKW 3s) using the Position Sensitive Proportional Counter on the ROSAT X-ray satellite. The images reveal smooth, symmetrical X-ray emission filling the cluster with a sharp peak on each central galaxy. The cluster surface brightness profiles can be decomposed using superposed King models for the central galaxy and the intracluster medium. The King model parameters for the cluster portions are consistent with previous observations of these clusters. The newly measured King model parameters for the central galaxies are typical of the X-ray surface brightness distributions of isolated elliptical galaxies.

Spatially resolved temperature measurements in annular rings throughout the clusters show a nearly isothermal profile. Temperatures are consistent with previously measured values, but are much better determined. There is no significant drop in temperature noted in the innermost bins where cooling flows are likely to be present, nor is any excess absorption by cold gas required. All cold gas columns are consistent with galactic foreground absorption.

We derive mass profiles for the clusters assuming both isothermal temperature profiles and cooling flow models with constant mass flow rates. Our results are consistent with previous Einstein IPC observations by Kriss, Cioffi, & Canizares, but extend the mass profiles out to 1 Mpc in these poor clusters.

Final technical report submitted to NASA for grant NAG5-1952.

Gerard A. Kriss
Principle Investigator
August 31, 1995

(NASA-CR-199320) A STUDY OF COOLING FLOWS IN POOR CLUSTERS OF GALAXIES Final Technical Report (JHU) 35 p

N96-13347

Unclas

G3/89 0065720

1. Introduction

The first-ranked galaxies of clusters are the most luminous standard candles available for studying the cosmic distance scale at high redshift (Schneider, Gunn & Hoessel 1983). Understanding the formation and evolution of these supergiant elliptical D and cD galaxies is important for validating their use as standard candles, and for understanding the dynamics of clusters of galaxies. The poor clusters containing central dominant galaxies identified by Morgan, Kaiser & White (1975; MKW) and Albert, White & Morgan (1977; AWM) are crucial keys to understanding the formation of cD galaxies. Any theory of the origin of cD galaxies must explain their presence in these poor clusters as well as their more common occurrence in rich clusters. While current opinion favors a process of mergers and galactic cannibalism following cluster virialization (e.g., Hausman & Ostriker 1978, or Richstone and Malumuth 1983), Merritt (1983, 1984) argues that cD's are otherwise normal giant ellipticals which have avoided tidal truncation by the cluster potential by virtue of their special location at the cluster center. The strong cooling flows typically associated with cD galaxies and the attendant formation of low mass stars could also account for a substantial fraction of the total galactic mass over the lifetime of the cluster (Fabian, Nulsen & Canizares 1984, 1991). Each of these mechanisms predicts that the dominant galaxy should lie at or near the dynamical center of its cluster. Strong cluster X-ray emission always peaks on these central galaxies (Jones & Forman 1984), suggesting that they lie at the bottom of the cluster potential well. Several kinematic studies, however, have discovered examples of cD's in *rich* clusters with high peculiar velocities relative to the cluster mean (Sharples, Ellis & Gray 1988; Hill et al. 1988; Malumuth et al. 1992). These high peculiar velocities may be due to mergers of sub-clusters, one of which contained the cD galaxy or its seed. Thus dominant galaxies in poor clusters may represent an early, pristine state of the dynamical evolution of a cD galaxy undisturbed by mergers with other sub-clusters.

The MKW and AWM poor clusters represent a smooth continuation in optical and X-ray properties from the richer Abell clusters (Bahcall 1980), and their central galaxies share many characteristics of their rich cluster cousins. The X-ray emission peaks on the dominant galaxy (Kriss et al. 1980; Kriss, Cioffi & Canizares 1983; KCC). The cooling time for the intracluster gas is short, and it accretes around and onto the central galaxy in a cooling flow (Canizares, Stewart & Fabian 1983; CSF). For those clusters with many measured velocities, the dominant galaxy also lies at the *kinematic* center of the cluster (Beers et al. 1984; Malumuth & Kriss 1986). Finally, apart from the lack of an extended optical envelope, the poor cluster dominant galaxies have optical morphologies and dynamical properties akin to the rich cluster cD's — large effective radii, low central surface brightness, and a high frequency of multiple nuclei (Thuan and Romanishin 1981; Malumuth & Kirshner 1981, 1985).

The brightest X-ray emitting poor clusters previously observed with the *Einstein Observatory* are ideally matched to the capabilities of the ROSAT PSPC —

- they have low temperatures well suited to the 0.1-2.5 keV bandpass of ROSAT,
- they have scale sizes for their cooling flows easily resolved with the PSPC, and
- they have high enough surface brightness to obtain spatially resolved spectra.

The improved spatial and spectral resolution of the PSPC and its higher sensitivity relative to the *Einstein* IPC (3 to 4 times more efficient at these temperatures) enables us to measure spatially resolved temperature profiles within the cooling cores of the clusters and to obtain globally averaged spectra over the 500 kpc to 1 Mpc range outside the cooling radius r_{cool}, the point where the gas cooling time equals the Hubble time.

2. The ROSAT Data

Three poor clusters were observed, all of which exhibit evidence of cooling flows (Canizares, Stewart, & Fabian 1983; Malmuth & Kriss 1986). Table 1 lists relevent properties of each cluster. Luminosities and distances here and throughout this report are calculated assuming $H_0 = 50$ km s^{-1} Mpc^{-1} and $q_0 = 0$. The cited column density is the expected Galactic column obtained via interpolation from the 21 cm H I survey of Stark et al. (1991) using the Einstein On-Line Service of the Smithsonian Astrophysical Observatory.

Observations were performed between December 1991 and August 1992 as summarized in Table 2. The tabulated observation length is the net time after filtering out data for which the MV rate was high (see below).

Table 1: Summary of General Properties of Observed Clusters

Name	α (B1950)	δ (B1950)	z	L_x (10^{43} ergs s^{-1})	Richness Class	log N_H (cm^{-2})
AWM4	16 02 48.9	+24 04 04	0.0322	3.30	−1	20.69
MKW3s	15 19 25.0	+07 53 13	0.0434	23.00	0	20.46
MKW4	12 01 53.3	+02 10 28	0.0200	2.30	−1	20.27

The data in this paper were originally received on tape in Flexible Image Transport System (FITS) format from NASA. They were then converted to files readable by the PROS X-ray analysis package for IRAF (version 2.3), and subsequent analysis was performed using the relevent parts of this package. In particular, the data were converted to QPOE files. A QPOE file is an event list which contains the following data for each event recorded by the PSPC detector: x coordinate, y coordinate, time, PHA bin and PI bin. These event list files can be manipulated as if they are image files with a resolution of 0.5 arcsec/pixel. However, when treated as image files, the QPOE data points are binned into 15" × 15" pixels.

The clusters examined here are the bright, diffuse objects located at the center of each image. All clusters except AWM4 are approximately circularly symmetric. AWM4 shows some ellipticity. Other X-ray sources are visible in each field, but have been excluded from analysis as described below. In the MKW3s image diffuse X-ray emission from a neighboring cluster is visible at the northeast edge of the field. The region where this diffuse source is located — between position angles $-20°$ and $40°$ from radius 30 arcmin to the edge of the field — was excluded entirely from analysis.

2.1. Initial Reduction Procedures

The first step in processing the data was to exclude unwanted non-cluster X-ray sources from analysis. The Standard Analysis Software System (SASS) analysis which accompanied the data included a master source list (MASOL) of possible X-ray sources imaged in each observation. Regions were defined surrounding those MASOL sources which could be visually verified. These regions were excluded in all subsequent calculations. These excluded sources are listed in Tables 3–5. The X and Y coordinates in the 15" binned images of each excluded source are listed as well as the radius in arcminutes of the excluded region surrounding each one.

Table 2: Observation Log

Name	Date of Observation	Length (s)	Root Name of Data Set
AWM4	26-JAN-92	18374	rp800129
MKW3s	15-AUG-92	8025	rp800128
MKW4	16-DEC-91	9751	rp800127

Table 3: Excluded Sources for AWM4

X	Y	Radius (arcminutes)
210.03	295.22	1.50
260.67	284.41	1.50
139.42	235.22	2.00
304.15	212.63	2.50
231.54	204.98	1.75
262.04	200.11	1.75
296.97	160.57	3.00

Table 4: Excluded Sources for MKW3s

X	Y	Radius (arcminutes)
267.37	432.86	2.50
237.10	339.67	2.00
145.55	332.81	2.50
251.41	314.68	1.50
239.33	308.60	1.50
182.87	307.64	2.50
457.96	294.33	7.50
317.98	268.30	1.50
322.72	215.44	1.75
293.70	206.08	1.50
149.03	158.10	3.50
378.14	118.27	6.25

Table 5: Excluded Sources for MKW4

X	Y	Radius (arcminutes)
255.40	96.00	44.00
306.02	400.53	4.00
368.24	385.70	3.50
324.40	329.19	1.50
176.75	318.85	2.00
74.00	310.69	3.00
328.83	254.25	2.00
390.78	239.31	3.50
269.37	210.71	1.75
261.68	198.95	1.75
306.83	177.19	2.00
160.89	177.18	2.25
283.28	146.18	3.00
286.80	289.31	1.50
238.38	284.99	1.50
274.26	246.48	1.50
243.59	229.85	1.50

2.2. X-ray Surface Brightness Extraction

By counting the number of events that lie in concentric rings on the image, it is possible to ascertain surface brightness as a function of radius for the data. This necessarily assumes that the clusters are circularly symmetric. The ellipticity in AWM4 is ignored in this analysis. Such calculations were performed using annuli of the following sizes:

10" rings out to 1',

30" rings from 1' to 8',

60" rings from 8' to 18', and

75" rings from 24' to 44'.

Data from PI bins 17–247 were used. These bins correspond to bins 5–34 for the spectral analysis with an energy range of 0.17–2.48 keV.

This procedure gives a raw value of counts per pixel as a function of radius. However, several corrections have to be made to the raw values obtained from simply counting events. These corrections are described in the following sections.

2.2.1. PSPC Particle Background

The first correction applied is the subtraction of the charged particle background. The background rate due to charged particles is spatially uniform across the detector and quite low. It has been parameterized as a function of Master Veto rate (Snowden *et al.* 1992; Plucinsky *et al.* 1993). As they note, the accepted event rate varies greatly and increases significantly for MV rates > 170. Hence, as suggested by Snowden *et al.* (1992,1994), data for which the MV rate exceeded 170 were excluded from all analysis. The expected particle background count rate is on the order of 3×10^{-12} counts s^{-1} arcsec^{-2} bin^{-1} (Snowden *et al.* 1992). The background extends to PI bin 370, and events in bins 260–370 are exclusively due to particles. Summed over bins 1–370, the expected background count rate is $\sim 10^{-9}$ counts s^{-1} arcsec^{-2}.

2.2.2. Exposure Maps

The second correction adjusts for the varying exposure time of pixels in a given image. Because of both spacecraft wobble and vignetting caused by the support structure, the

total exposure time varies from pixel to pixel and will vary from observation to observation. However, the observational data can be used in conjunction with positional data from the telescope to create an exposure map. This exposure map can, in turn, be applied during data processing to correct for vignetting and for wobble. Since the charged particle background is not vignetted, it is important to apply exposure map corrections after the particle background has been subtracted.

Unfortunately, the original exposure maps created by SASS do not correct for vignetting properly at large radial distances from the field center. Thus, new exposure maps were made using programs written by S. L. Snowden based on analysis procedures suggested in his paper on extended object analysis with ROSAT (Snowden *et al.* 1994). These exposure maps have pixel sizes of 14".947 x 14".947, which are very close to the SASS pixel sizes of 15" x 15". Thus, in the data presented here, this pixel size difference is ignored.

2.2.3. Cosmic X-ray Background

After the particle background is subtracted and the exposure maps are used to correct for varying exposure time, the cosmic X-ray background also must be subtracted. It is difficult to accurately determine the background for several reasons. Other sources in the field can contribute to the background in a nonuniform manner. Background also varies as a function of spacecraft position over the exposure time of the image.

For these calculations, background determination is handled by fitting the background as a free parameter in the King models (discussed below) to obtain a first approximation best fit. The background value obtained from this analysis was then used as a fixed background for subsequent calculations.

3. X-ray Surface Brightness Models

A well-resolved X-ray surface brightness profile can provide a great deal of information about a cluster. Because the surface brightness is directly related to the density of the intracluster gas, the density of gas as a function of radius can be obtained. Consequently, gas mass as a function of radius may be determined, giving insight into the "missing mass" problem.

A number of density models have been proposed. One of the most versatile is the analytic model proposed by King (1962). Originally developed as a model of galaxy density in clusters, the King model has been used with considerable success as a model of X-ray

surface brightness (Jones & Forman 1984).

We have used a sum of two King models to fit the X-ray surface brightness. Physically, one King model describes the emission associated with the gas in the cluster potential well. A second, inner model describes the emission associated with gas in the potential well of the large (cD) galaxy at the center of the cluster. To describe the volume emissivity of the X-ray emitting gas we set

$$E_{x,tot}(r) = E_{x1}[1 + (\frac{r}{r_{c1}})^2]^{-3\beta_1} + E_{x2}[1 + (\frac{r}{r_{c2}})^2]^{-3\beta_2}. \quad (1)$$

The subscript 1 indicates values for the central galaxy potential well and subscript 2 indicates values associated with the cluster potential well. The volume emissivity is numerically projected onto the sky and then convolved with the PSPC point response function, which is assumed to be a Gaussian of dispersion 10.5 arcsec. For the final fitting, there were six free parameters: E_{x1}, E_{x2}, r_{c1}, r_{c2}, β_1 and β_2. Background was used as a free parameter initially and then fixed before final fitting was done. Because of uncertainties in the background, data taken beyond 21 arcmin are not used in the fitting. Figures 1–3 show the observed and fitted X-ray surface brightness profiles. The solid lines indicate the modelled X-ray surface brightness. Tables 6–8 list the parameters determined to provide the best fit for each data set. Degrees of freedom are listed explicitly because the number of usable data points varies from cluster to cluster.

For core radius values, angular diameters were converted to Mpc by using the small angle approximation after calculating the distance to each cluster. Distances to the clusters were calculated using the angular diameter distance

$$d_c = cz\frac{(1 + z/2)}{H_0(1 + z)^2}\ , \quad (2)$$

where c is the speed of light, z is the cluster redshift, and $H_0 = 50$ km s^{-1} Mpc^{-1}. A flat geometry is assumed, so the deceleration parameter q_0 is taken to be zero.

As the figures indicate, a sum of two King models provides a reasonable description of the X-ray surface brightness for all the clusters. A wide range of core radii (0.01–1.10 Mpc) has been observed for clusters of galaxies, and values of β typically lie between 0.40 and 1.00. All of the calculated core radii and β's presented here fall within these ranges.

All of these clusters were previously observed by the *Einstein Observatory*, and they all have been fitted to King models. Table 9 lists values obtained by Kriss et al. (1983) for the cluster core radius (r_{c2}). β_2 was assumed to be 1.00 in these previous fits. Our new results compare well with previously derived values for all three cluster. Our values for the core radii of clusters MKW3s and MKW4 do not fall within the range of previously

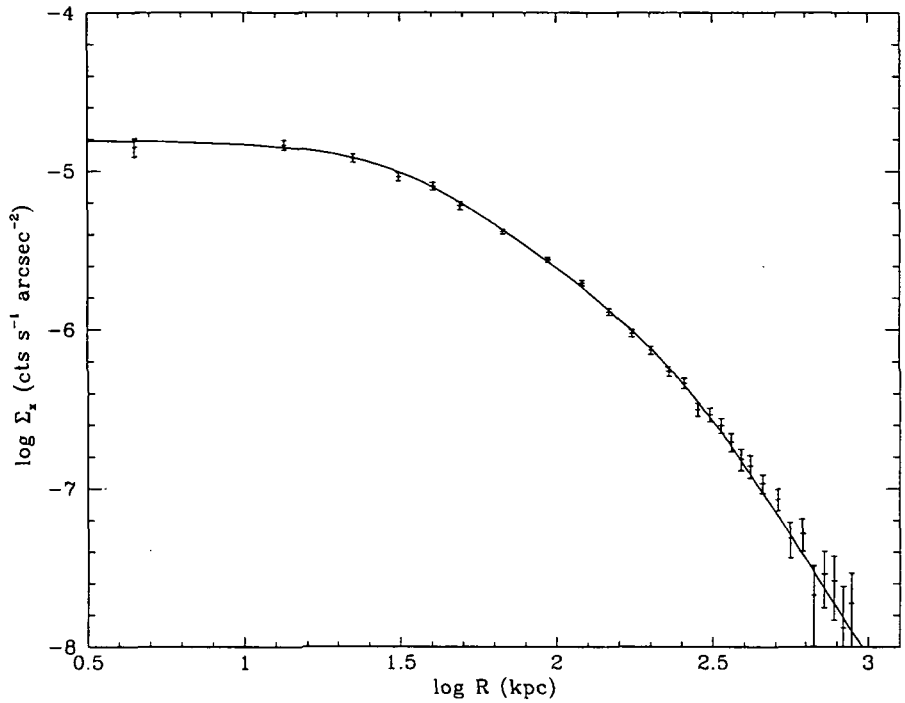

Fig. 1.— X-ray Surface Brightness Profile of AWM4. The data points are crosses with 1σ error bars. The best fit profile is the solid line.

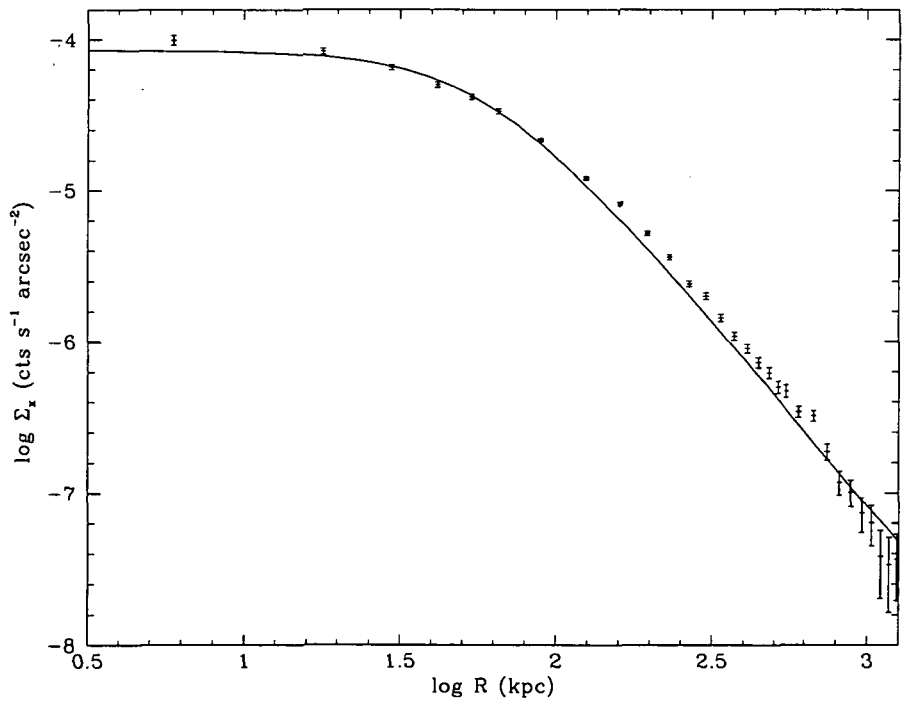

Fig. 2.— X-ray Surface Brightness Profile of MKW3s. The data points are crosses with 1σ error bars. The best fit profile is the solid line.

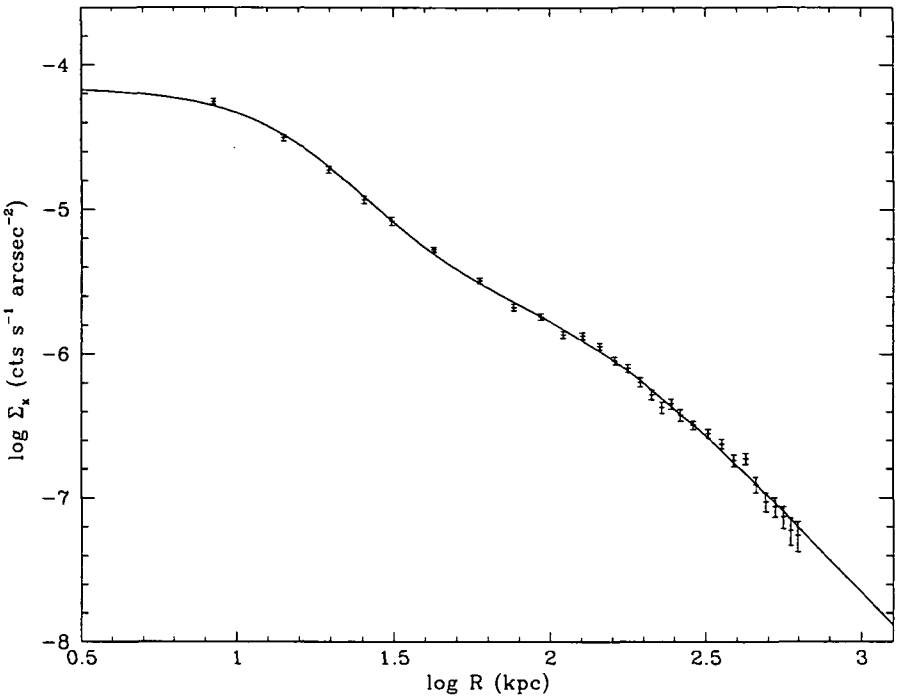

Fig. 3.— X-ray Surface Brightness Profile of MKW4. The data points are crosses with 1σ error bars. The best fit profile is the solid line.

Table 6: King Model Best Fit Values for AWM4

Parameter	Value
E_{x1} (10^{-7} cts s^{-1} $arcsec^{-3}$)	4.263
r_{c1} (arcsec)	42.18
r_{c1} (kpc)	37.73
β_1	0.586
E_{x2} (10^{-7} cts s^{-1} $arcsec^{-3}$)	0.1195
r_{c2} (arcsec)	227.3
r_{c2} (kpc)	203.3
β_2	0.789
Background (10^{-7} cts s^{-1} $arcsec^{-2}$)	5.022
$\dot{M}$	-52.434
χ^2	31.19
Degrees of Freedom	24

Table 7: King Model Best Fit Values for MKW3s

Parameter	Value
E_{x1} (10^{-7} cts s^{-1} $arcsec^{-3}$)	22.62
r_{c1} (arcsec)	45.75
r_{c1} (kpc)	54.21
β_1	0.570
E_{x2} (10^{-7} cts s^{-1} $arcsec^{-3}$)	0.2300
r_{c2} (arcsec)	243.7
r_{c2} (kpc)	288.8
β_2	0.918
Background (10^{-7} cts s^{-1} $arcsec^{-2}$)	5.004
$\dot{M}$	-135.983
χ^2	42.22
Degrees of Freedom	25

Table 8: King Model Best Fit Values for MKW4

Parameter	Value
E_{x1} (10^{-7} cts s^{-1} $arcsec^{-3}$)	74.84
r_{c1} (arcsec)	17.75
r_{c1} (kpc)	10.02
β_1	0.590
E_{x2} (10^{-7} cts s^{-1} $arcsec^{-3}$)	0.1095
r_{c2} (arcsec)	226.1
r_{c2} (Mpc)	127.6
β_2	0.542
Background (10^{-7} cts s^{-1} $arcsec^{-2}$)	4.148
$\dot{M}$	-85.043
χ^2	36.46
Degrees of Freedom	25

measured values, but they are reasonably close. Some portion of the discrepancy is due to the fact that all previous models use β as a fixed parameter. In addition, previous analyses fit the data to a single King model rather than to two King models. These two factors seem sufficient to explain the differences between ours and previous results for all cases. However, Kriss *et al.* also note that the values they give for the core radii of the poor clusters may be an artifact of the *Einstein Observatory*'s IPC resolution and the depth of each exposure rather than a true measure of scale.

No previous values for r_{c1} and β_1 have been obtained for these clusters. One expects a much shallower potential well for the central galaxy than for the cluster as a whole. Velocity dispersions of cD galaxies are typically $\sim$ 300 km s^{-1} (Malumuth & Kirshner 1981), while cluster velocity dispersions are $\sim$ 500-1000 km s^{-1} (*e.g.*, Bahcall 1981). Since the gas temperature is assumed to be the same over all regions in these models, one expects β_1 to be less than β_2 in general. Only MKW4 deviates from this expectation.

Although X-ray surface brightness profiles of the central galaxies in clusters are not available for comparison, X-ray surface brightness profiles of elliptical galaxies have been fit to King models. For elliptical galaxies, typical core radii lie between 1 and 26 kpc, with the 90% confidence range of the largest galaxies observed extending to $\sim$ 60 kpc (Forman *et al.* 1985; Trincheri *et al.* 1985). The index β for elliptical galaxies is $\sim$ .5 on average, with a typical range of .4–.7. All of our fits give values which fall within the range of previously measured core radius and β values for ellipticals, so we believe that our models are good descriptions of the central galaxy potentials in the clusters we have observed.

Table 9: Previous X-Ray Surface Brightness Results

Cluster Name	Previously Obtained r_{c2} (Mpc)	Previously Obtained β_2
AWM4	0.15–0.22	1.00*
MKW3s	0.15–0.22	1.00*
MKW4	0.15–0.22	1.00*

* indicates an assumed rather than calculated value of β.

4. Spectral Analysis

Spectral analysis of X-ray data can be used to obtain the temperature of the intracluster gas. If such data is well resolved spatially, then the temperature can be determined as a function of radius. We have used Raymond & Smith (1977) thermal models as implemented in the PROS package to fit the spectral data.

For each cluster of galaxies observed, spectra were extracted in annular rings using the IRAF PROS package. Although the PSPC detector has 256 PI channels, these are binned into 34 channels for spectral analysis. Table 10 gives the energy range and channels included for each of the 34 spectral bins. Annuli were defined in such a way that the total number of counts in each ring would be approximately equal. Thus, their sizes vary from cluster to cluster. Table 11 lists the annuli selected. In addition to these, spectra were extracted and analyzed for the region 0–18 arcmin for each data set to obtain a cluster "mean" temperature. An annulus of inner radius 24 arcmin and outer radius 44 arcmin was used as a basis for the X-ray background.

The charged particle background is corrected for in the PROS package using the methods presented by Plucinsky *et al.* (1993). However, the background correction method used is not valid over all PI channels due to the gas contamination. For all observations, spectral bins 1–5 were excluded from fitting. Times for which the MV rate exceeded 170 were also excluded from analysis.

After spectra are extracted, they can be fitted to Raymond–Smith models in order to determine temperature as a function of radius. Temperature, line-of-sight neutral hydrogen column density, and normalization are the free parameters for these fits. Heavy element abundance is also a parameter for fitting, and preliminary fits were made varying this parameter. Once a reasonable value was obtained for the heavy element abundance, that value was used as a fixed parameter for the final fit. Heavy element abundance is assumed to be constant over the entire cluster. Tables 3.3–3.5 list the best-fit results. For these models there were 26 degrees of freedom (29 data points - 3 free parameters). The heavy element abundance range is the 90% confidence range in percent solar abundance.

Figures 4–6 show the best-fit temperatures plotted as a function of radius for each observation. Figures 7–9 show the best-fit neutral hydrogen columns as a function of radius. Error bars on these figures are at the 90% confidence level.

As an examination of the tables show, the Raymond–Smith thermal model fits all the extracted spectra acceptably except for the central region of MKW3s. In general, the lower the signal-to-noise ratio for the observation, the better the fit. Poor fits to the 0–18 arcmin cluster mean spectra are to be expected since temperature will vary as a function of radius.

Table 10: Bins Used for Spectral Analysis

34-bin number	Energy Low-High (keV)	256-channels included	34-bin number	Energy Low-High (keV)	256-channels included
1*	0.07–0.09	7–8	18	0.84–0.91	84–90
2*	0.09–0.11	9–10	19	0.91–0.99	91–98
3*	0.11–0.14	11–13	20	0.99–1.07	99–106
4*	0.14–0.17	14–16	21	1.07–1.15	107–114
5*	0.17–0.20	17–19	22	1.15–1.23	115–122
6	0.20–0.24	20–23	23	1.23–1.32	123–131
7	0.24–0.28	24–27	24	1.32–1.41	132–140
8	0.28–0.32	28–31	25	1.41–1.50	141–149
9	0.32–0.37	32–36	26	1.50–1.60	150–159
10	0.37–0.42	37–41	27	1.60–1.70	160–169
11	0.42–0.47	42–46	28	1.70–1.80	170–179
12	0.47–0.52	47–51	29	1.80–1.91	180–190
13	0.52–0.58	52–57	30	1.91–2.02	191–201
14	0.58–0.64	58–63	31	2.02–2.13	202–212
15	0.64–0.70	64–69	32	2.13–2.24	213–223
16	0.70–0.77	70–76	33	2.24–2.36	224–235
17	0.77–0.84	77–83	34	2.36–2.48	236–247

* Excluded from analysis

Table 11: Annuli Selected for Extraction of Spectra

Cluster	Radii (arcmin)
AWM4	0–2
	2–5
	5–18
MKW3s	0–2
	2–4
	4–18
MKW4	0–2
	2–4
	4–6.5
	6.5–10.5
	10.5–18

Table 12: AWM4 Spectral Best Fit Results

Heavy Element Abundance = 50% Solar

Region (arcmin)	kT (keV)	90% Conf. Range	$\log(N_H)$	90% Confidence Range	Elemental Abundance Range	χ^2	$P(>\chi^2)$
0–18	1.69	1.5–2.1	20.79	20.68–20.92	20–90	27.69	0.40
0–2	1.67	1.4–2.2	20.82	20.76–20.90	20–110	19.60	0.80
2–5	1.91	1.5–2.7	20.75	20.66–20.84	10–90	21.85	0.70
5–18	1.54	1.3–2.4	20.67	20.45–20.10	20–500	23.30	0.60

Table 13: MKW3s Spectral Best Fit Results

Heavy Element Abundance = 50% Solar

Region (arcmin)	kT (keV)	90% Conf. Range	$\log(N_H)$	90% Confidence Range	Elemental Abundance Range	χ^2	$P(>\chi^2)$
0–18	3.22	2.4–4.4	20.40	20.35–20.45	10–70	22.77	0.65
0–2	3.41	2.4–5.0	20.47	20.43–20.50	10–90	36.37	0.10
2–4	5.12	2.9–8+	20.39	20.32–20.45	10–500	18.56	0.85
4–18	1.68	1.2–3.6	20.17	19.96–20.33	10–80	22.65	0.75

Table 14: MKW4 Spectral Best Fit Results

Heavy Element Abundance = 75% Solar

Region (arcmin)	kT (keV)	90% Conf. Range	$\log(N_H)$	90% Confidence Range	Elemental Abundance Range	χ^2	$P(>\chi^2)$
0–18	1.35	1.30–1.45	20.20	20.13–20.27	50–90	30.08	0.25
0–2	1.22	1.16–1.29	20.35	20.28–20.41	70–300	27.80	0.35
2–4	2.08	1.5–4.1	20.22	20.11–20.31	20–500	16.13	0.90
4–6.5	1.65	1.3–2.5	20.23	20.10–20.35	20–140	15.91	0.90
6.5–10.5	1.32	1.15–1.70	19.95	19.78–20.10	10–80	26.23	0.45
10.5–18	1.21	1.10–1.50	19.91	19.45–20.25	10–140	23.22	0.60

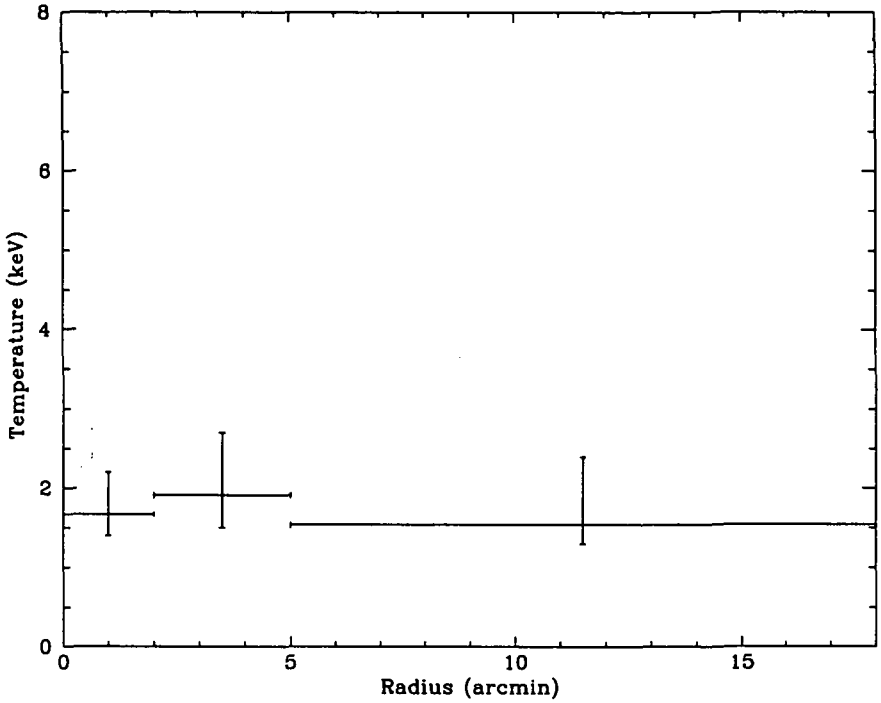

Fig. 4.— Temperature versus Radius for AWM4

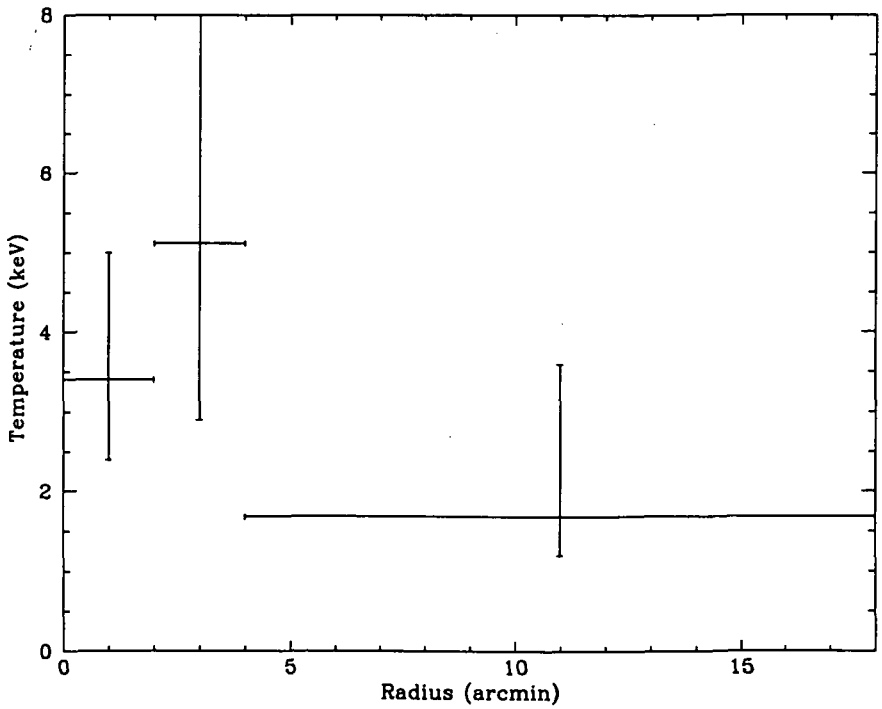

Fig. 5.— Temperature versus Radius for MKW3s

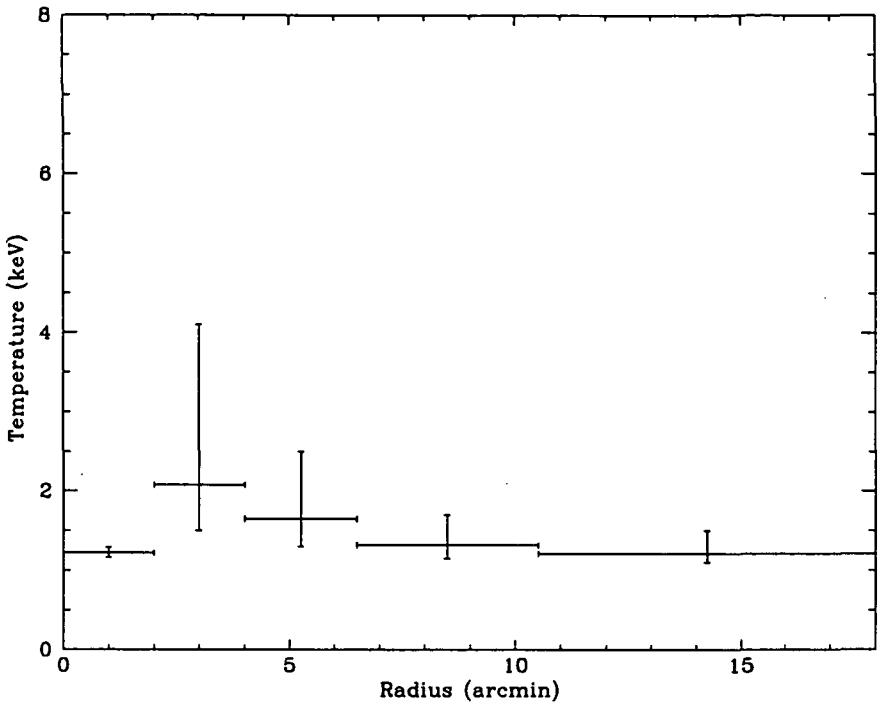

Fig. 6.— Temperature versus Radius for MKW4

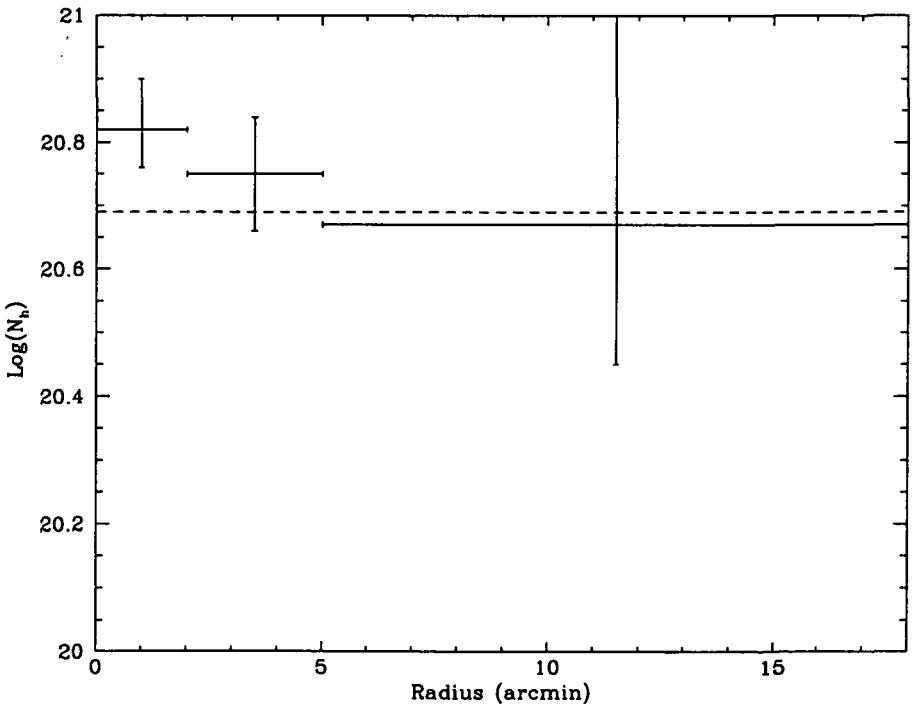

Fig. 7.— Log(N_H) versus Radius for AWM4

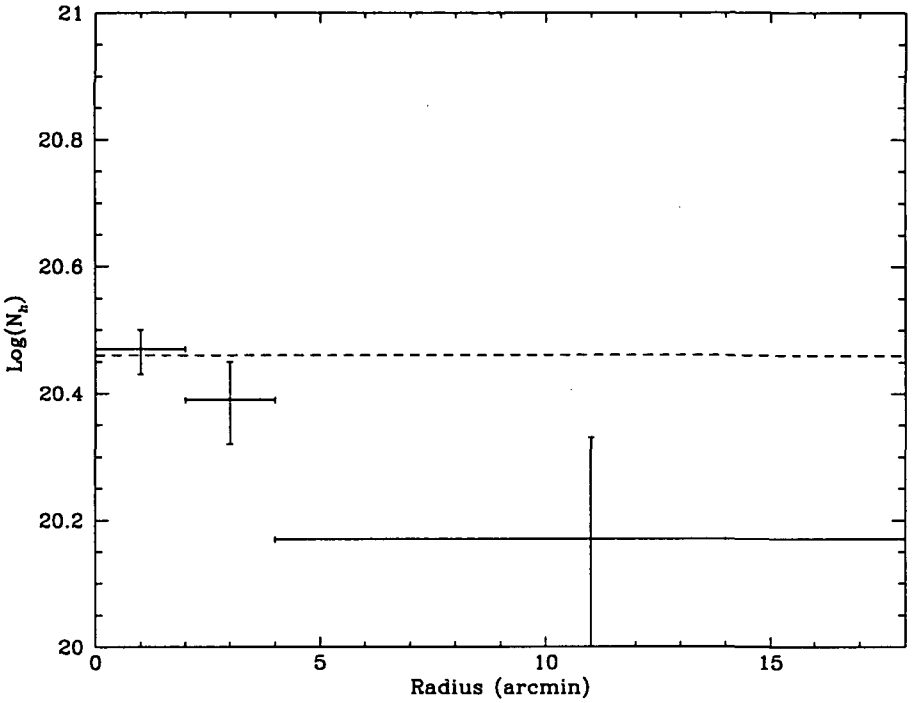

Fig. 8.— Log(N_H) versus Radius for MKW3s

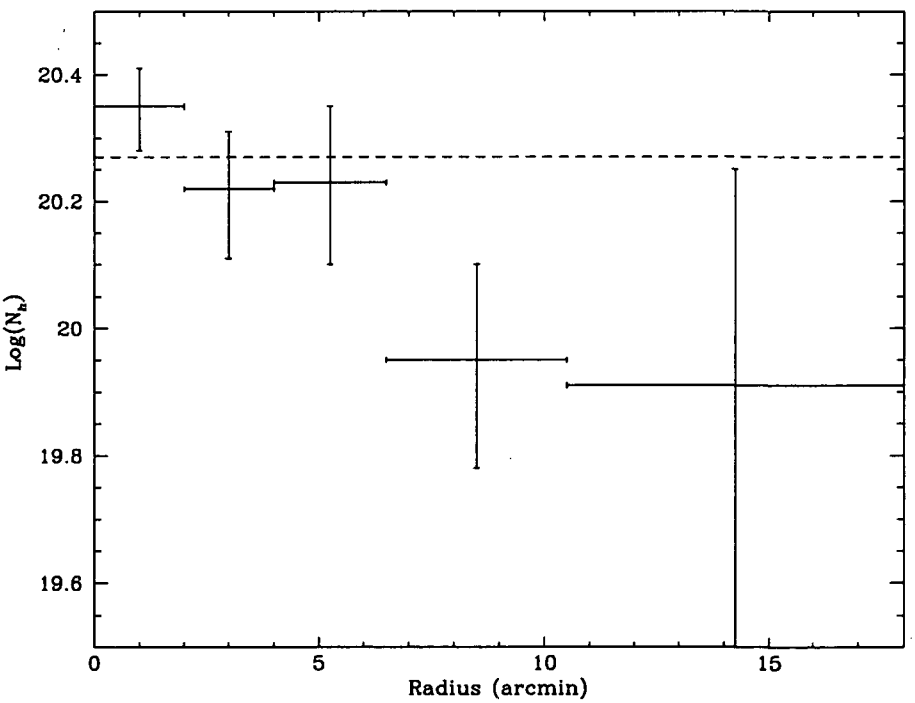

Fig. 9.— Log(N_H) versus Radius for MKW4

There is better agreement between the data and the model for the annular regions.

For MKW3s the fit in the central (0 to 2 arcmin) region is poor. Possible reasons for this include

- Emission received from the innermost region includes both emission from the cluster gas and from the central cD galaxies;
- a cooling flow in this region would cause a thermal gradient, precluding a reasonable single temperature fit.
- Projection effects may cause a poor fit. Emission from the center of the image does not come only from the center of the cluster. Rather, emission from all radii along the line of sight to the cluster center are superimposed on each other.
- Heavy element abundance may vary within the gas, and the abundance used in the model may be inappropriate for the central region.

Although one would like somewhat closer agreement between observation and prediction, the Raymond–Smith models provide reasonable fits in general. Except in the region discussed above, no χ^2 exceeds 30, and in most cases χ^2 is less than 26.

Comparison of expected galactic N_H with the modelled N_H shows some discrepancy. A higher column density than expected could be due to cold gas within the intracluster medium (White et al. 1991), but in several cases, a lower column density than expected proved to give the best fit. For MKW3s and MKW4 the upper limit on the modelled N_H was lower than the expected column density for more than half of the annular regions. The most likely explanation for this is that the X-ray background is ill-determined. As described earlier, the region used to define the background was an annulus of inner radius 24 arcmin and outer radius 44 arcmin. If the calculated background were too low for any reason, the best fit galactic hydrogen column density would also be lower than it should be. Tests on the data show that a 1% change in the background results in a change in the best fit $\log(N_H)$ value of ~ 0.1, with the 90% confidence range changing similarly.

Temperature, on the other hand, does not change significantly with small changes in the background level (< 0.08 keV change for a 1% change in the background), so the best-fit temperature as a function of radius may be considered reasonable, if not always well constrained. In no case do the data contradict the hypothesis that there is a cooling flow at the center of each cluster, but there is also no direct evidence to support the existence of cooling flows in AWM4 or in MKW3s. In MKW4, there is some indication that the

central regions are cooler than outer regions, but the large error bars on the data make this evidence weak at best.

5. Cluster Mass Distributions

5.1. Density Profiles and the Gas Mass

Particle density profiles can be determined from emissivity models in a straightforward manner. Effective photon emissivity $C(n,T)$ is a function of density and temperature obtained by integrating the photon spectrum of the gas over the effective area of the detector. It has the following form:

$$C(n,T) = \frac{1}{4\pi D^2} \int \frac{n^2 \epsilon(E,T)}{E} A E e^{-N_H \sigma(E)} \, dE. \tag{3}$$

Here, n is the total particle density, $n^2\epsilon(E,T)/E$ gives the photon emissivity of the gas, $A(E)$ is the effective area of the detector, and N_H is the galactic neutral hydrogen density. $\sigma(E)$ is the total cross section to X-ray absorption, which is calculated using the cross sections and abundances of Morrison & McCammon (1983).

To compute the density profiles, the above equation was solved for n using values of $C(n,T)$ computed from the best fit emissivity models obtained in §3. We assume that all clusters are spherical and that all clusters are isothermal. The best fit temperatures for the 0–18 arcmin spectra were used throughout. Galactic neutral hydrogen densities were taken from Table 1. In equation 3 $C(n,T)$ is in units of counts cm^{-3} s^{-1}, so the King model normalization parameters first had to be converted to these units from counts arcsec^{-3} s^{-1}. Figures 10–12 show the radial density profiles for the clusters. A dotted line represents the contribution from the central galaxy; a dashed line represents the contribution from the intracluster gas; and a solid line represents the total gas density. Note that at small radii, the density of the intracluster gas is much less than that of the gas trapped by the central galaxy, while the central galaxy gas density drops at large radii.

Next, the total gas mass as a function of radius was obtained by numerically integrating the density profiles. A mean particle mass of $0.6m_p$ was assumed. Figures 13–15 show the integrated gas masses.

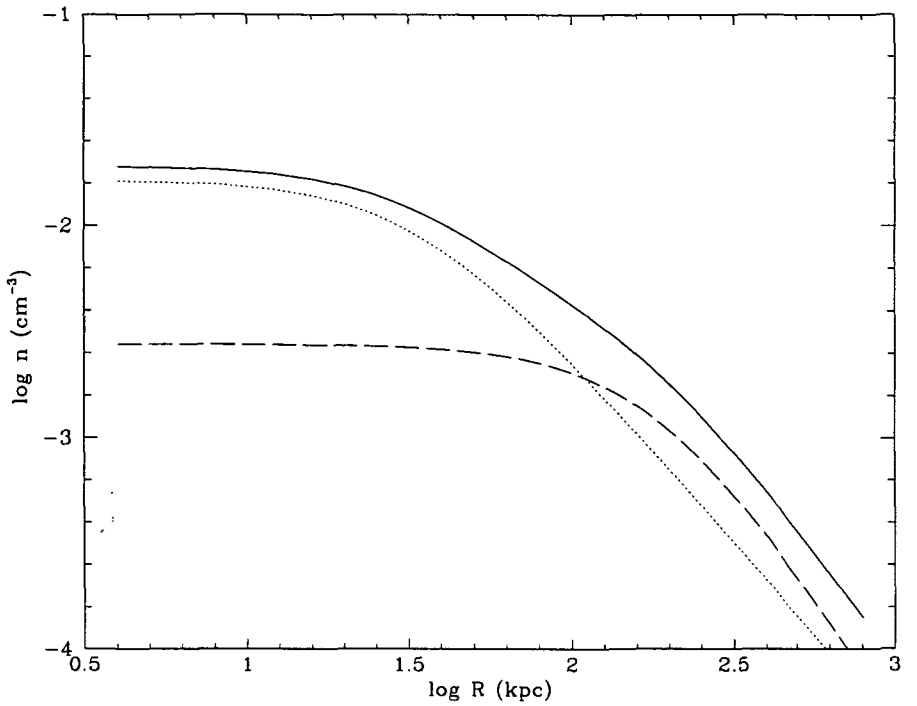

Fig. 10.— Gas Density in AWM4. The dotted line is the modelled contribution from the central galaxy. The dashed line represents the intracluster medium. The sum of the two produces the solid line.

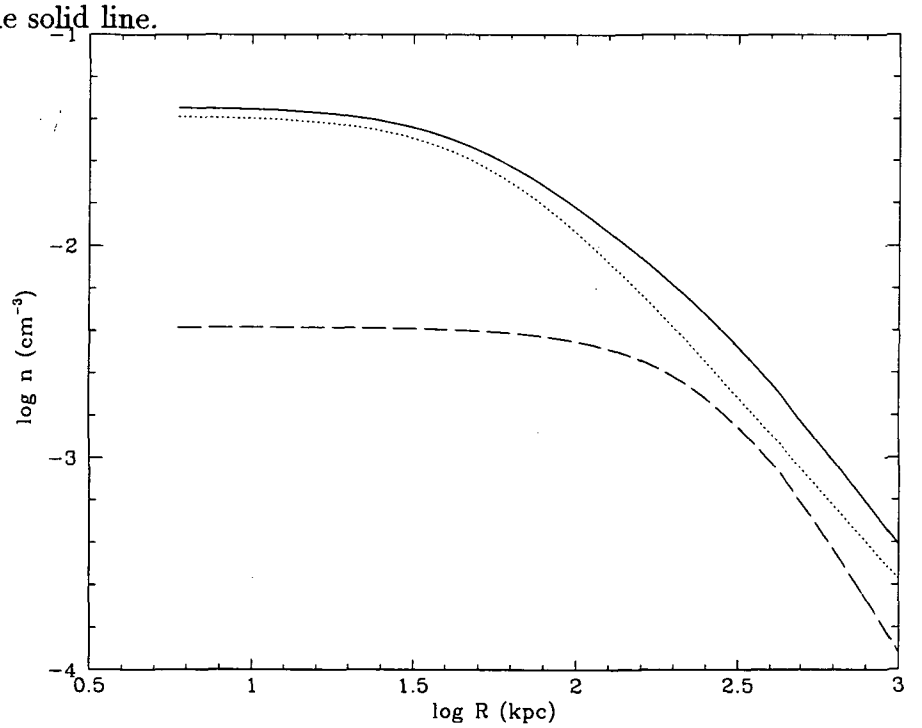

Fig. 11.— Gas Density in MKW3s. The dotted line is the modelled contribution from the central galaxy. The dashed line represents the intracluster medium. The sum of the two produces the solid line.

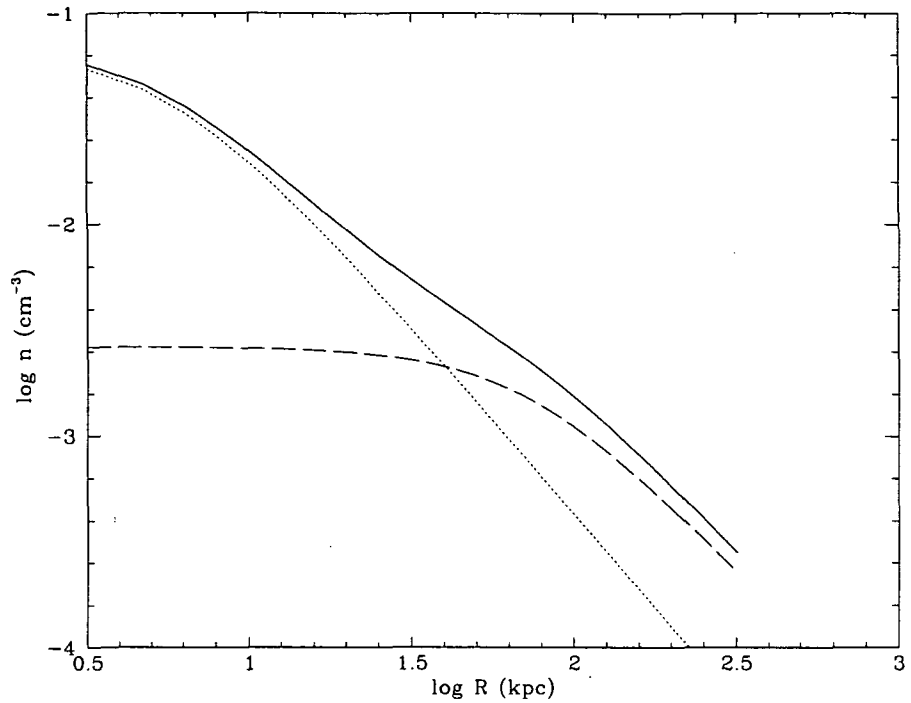

Fig. 12.— Gas Density in MKW4. The dotted line is the modelled contribution from the central galaxy. The dashed line represents the intracluster medium. The sum of the two produces the solid line.

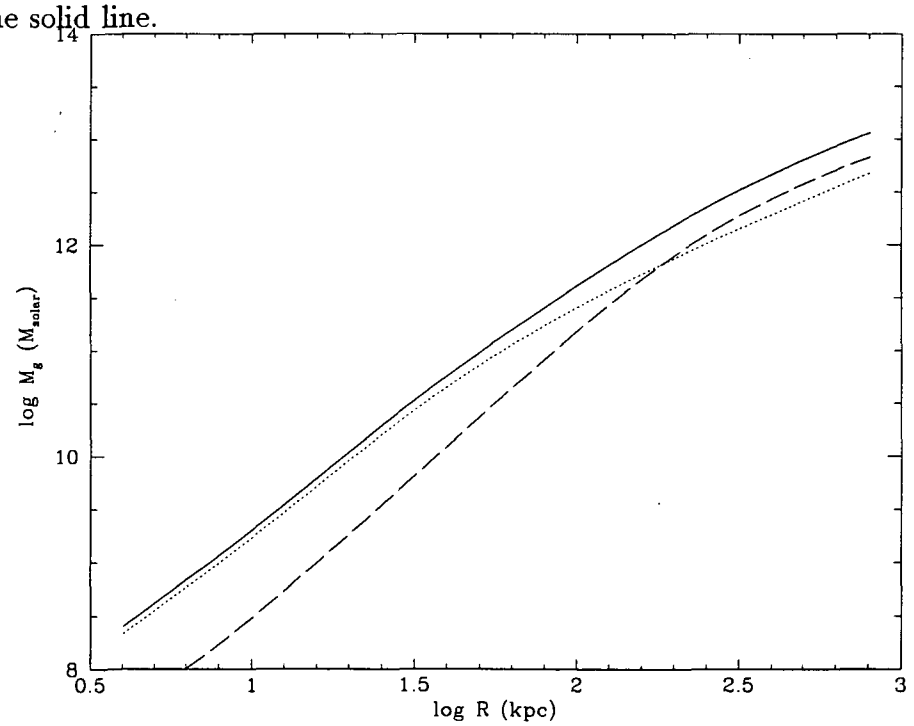

Fig. 13.— Integrated Gas Mass in AWM4. As before, the dotted line is the modelled contribution from the central galaxy. The dashed line represents the intracluster medium. The sum of the two produces the solid line.

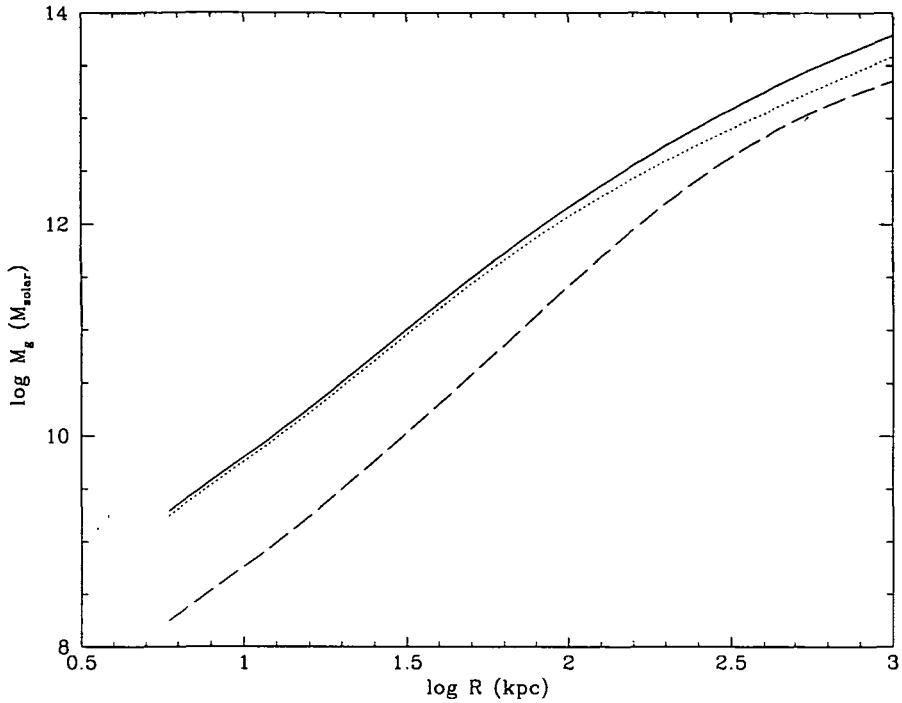

Fig. 14.— Integrated Gas Mass in MKW3s. As before, the dotted line is the modelled contribution from the central galaxy. The dashed line represents the intracluster medium. The sum of the two produces the solid line.

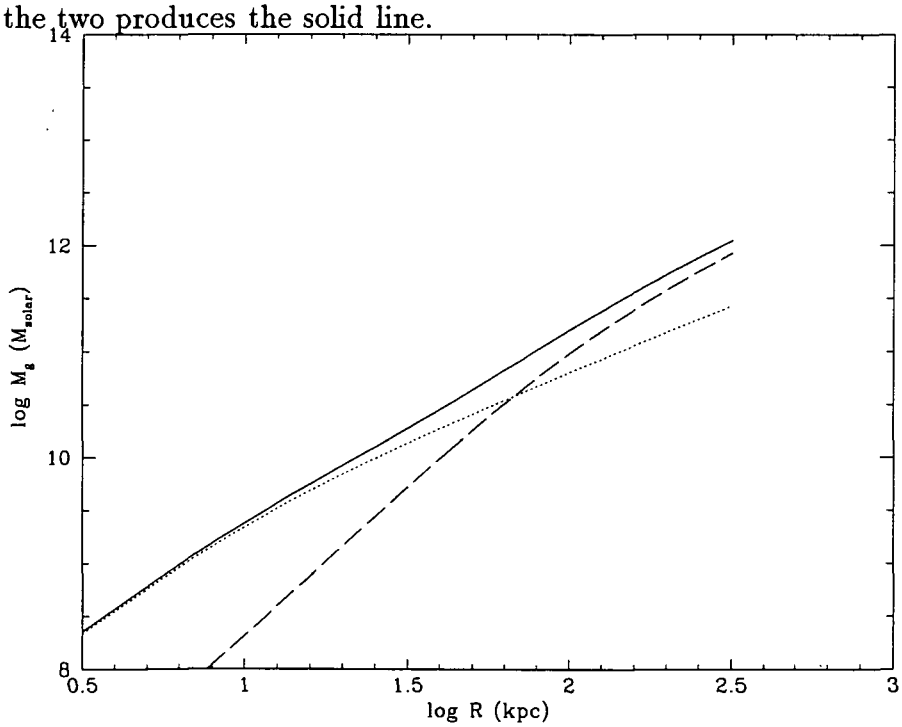

Fig. 15.— Integrated Gas Mass in MKW4. As before, the dotted line is the modelled contribution from the central galaxy. The dashed line represents the intracluster medium. The sum of the two produces the solid line.

5.2. Binding Masses

If the clusters are assumed to be isothermal spheres in hydrostatic equilibrium, binding masses can be calculated from density data using the hydrostatic equation, which can be written as

$$M(R) = \frac{-kT}{G\mu m_p}\left(\frac{d\ln n}{d\ln R} + \frac{d\ln T}{d\ln R}\right)R. \quad (4)$$

We take the clusters to be isothermal, so the logarithmic derivative of T is 0. M scales approximately linearly with R. Figures 16–18 show the binding masses as a function of radius.

5.3. Comparison to Previous Results

The gas densities and masses and the binding masses calculated here agree well with previous results. Table 15 compares these results with previously measured gas masses and binding masses. Values are given at a radius of 500 kpc. Previous poor cluster values are from Kriss *et al.* (1983).

Given that the uncertainties for both our calculations and the previous calculations are $\sim$ 30–50%, our values are in excellent agreement with previously obtained values for all clusters observed. Differences may be due to the fact that β was assumed to be 1 in previous results plus the higher sensitivity and better spatial resolution of the ROSAT PSPC.

5.4. Cooling Times

Cooling times for the gas in the clusters can be calculated as

Table 15: Comparison of Masses with Previous Results

	$M_g(10^{12}M_\odot)$		$M_b(10^{12}M_\odot)$	
Cluster	Our Results	Previous Results	Our Results	Previous Results
AWM4	10	5.5	56	52
MKW3s	14	14	109	73
MKW4	2.1	2.8	38	35

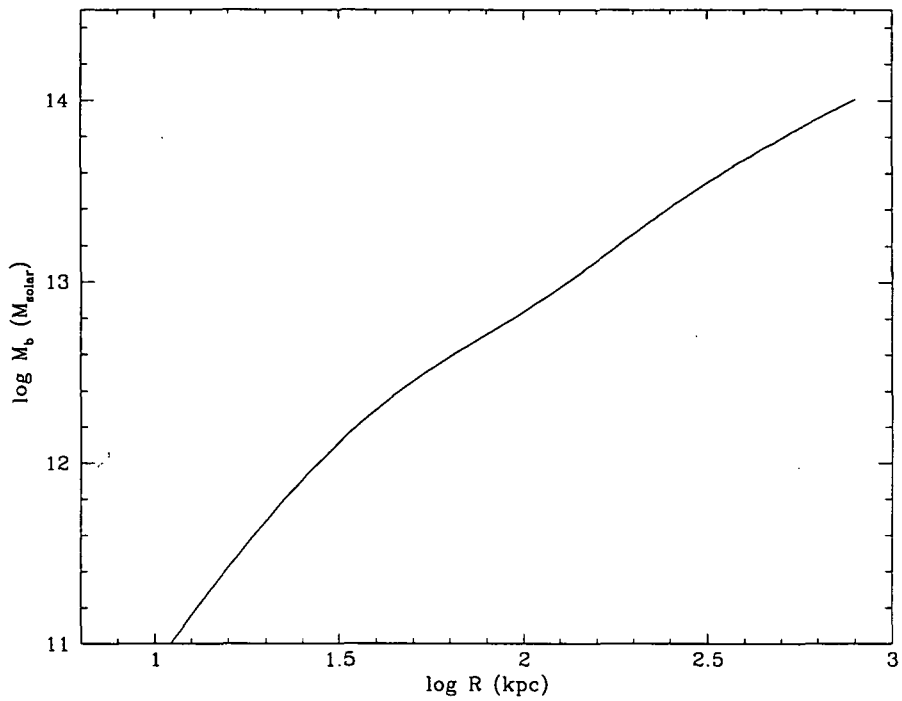

Fig. 16.— Binding Mass in AWM4

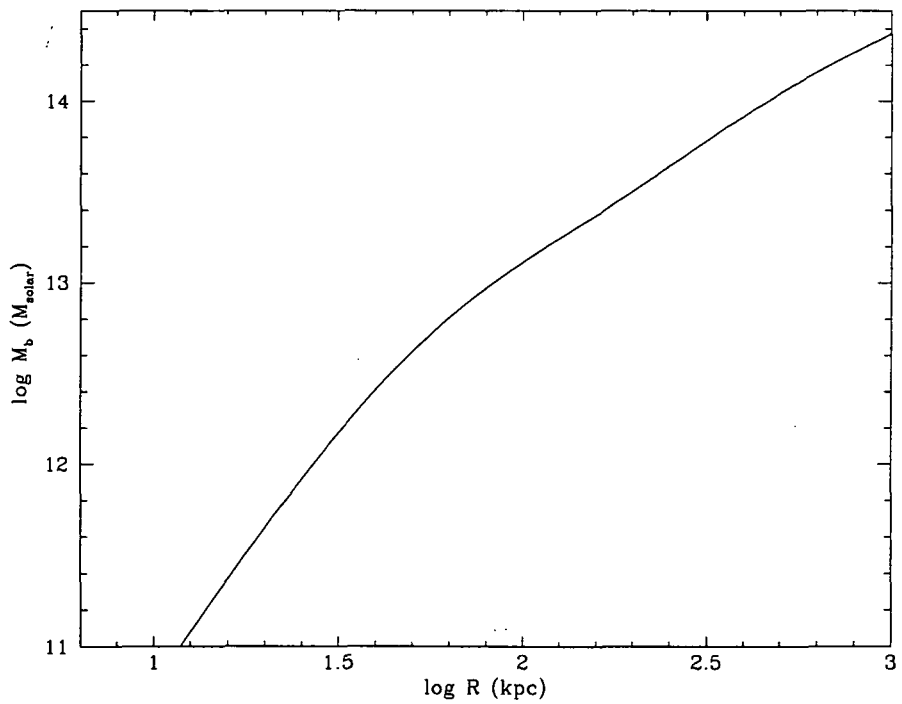

Fig. 17.— Binding Mass in MKW3s

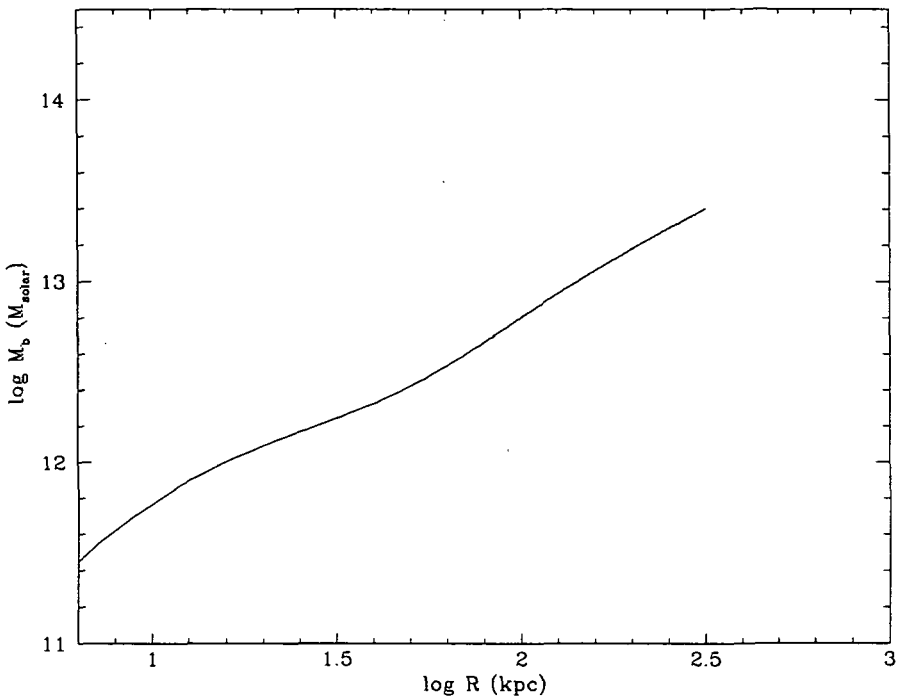

Fig. 18.— Binding Mass in MKW4

Table 16: Maximum Radius for $t_{cool} < t_H$

Cluster	r_{max} (kpc)
AWM4	273
MKW3s	290
MKW4	231

$$t_{cool} = \frac{3/2nkT}{n_e n_H \Omega(T)} = \frac{3.33 \times 10^{10}\mathrm{yr}(T/1\mathrm{keV})}{(\mathrm{n}/10^{-3}\ \mathrm{cm}^{-3})(\Omega/10^{-23})} \tag{5}$$

where n is the total particle density and $\Omega(T)$ is the cooling function as given by Raymond *et al.* (1976). Table 16 lists the maximum radius for which t_{cool} is less than the Hubble time t_H. ($t_H = 2 \times 10^{10}$ years for $H_0 = 50$ km s^{-1} Mpc^{-1}.) For each observation, t_{cool} is less than t_H for the innermost region of the cluster.

6. Cooling Flow Models

We have modeled the X-ray surface brightness and temperature profiles of the clusters using cooling flow models based on a constant mass flow rate. For a constant mass flow rate, and assuming spherical symmetry and quasi-hydrostatic equilibrium, it is possible to directly solve the cooling flow equations to obtain the binding mass profile of the cluster. The assumption of spherical symmetry will not greatly affect the resulting mass profile even in clusters with slight ellipticity (Fabian et al. 1981; Fabricant, Rybicki, & Gorenstein 1984; Cowie, Henriksen, & Mushotzky 1987). Unlike Fabian et al. (1984) (and references therein), however, we do not assume anything about the form of the gravitational potential. An X-ray surface brightness profile, a the spatially resolved temperature measurements, and the cooling flow assumptions fully specify the temperature and density profiles and thus the mass distribution.

For a steady-state cooling flow with a constant mass flow rate, the hydrodynamic equations are

$$\dot{M} = 4\pi r^2 \rho v, \tag{6}$$

$$-\frac{\partial p}{\partial r} = \rho \frac{\partial \phi}{\partial r}, \tag{7}$$

$$\frac{1}{r^2}\frac{\partial}{\partial r}\left[\frac{\gamma}{(\gamma-1)} pvr^2 + \rho v r^2 \phi + r^2 \kappa T^{5/2} \frac{\partial T}{\partial r}\right] = -n_e n_H \Lambda(T), \tag{8}$$

where $\dot{M}$ is the mass flow rate (positive outwards), r is the radius, ρ is the mass density of the gas, v is the bulk flow velocity of the gas, p is the gas pressure, ϕ is the gravitational potential, γ is the ratio of specific heats for the gas, κ is the conduction parameter, T is the gas temperature, n_e and n_H are the number densities of electrons and hydrogen atoms, and $\Lambda(T)$ is the radiative cooling function of the gas.

One can solve this system to obtain a differential equation for the temperature distribution —

$$\frac{\partial}{\partial r}\left[r^2\kappa T^{5/2}\frac{\partial T}{\partial r}\right] = -r^2 n^2 \Lambda(T) + \frac{\dot{M}k}{4\pi\mu m_H}\left[\frac{T}{n}\frac{\partial n}{\partial r} - \frac{1}{\gamma-1}\frac{\partial T}{\partial r}\right]. \quad (9)$$

We have converted the mass density ρ to the total particle density n as $\rho = \mu m_H n$, where μm_H is the mean mass per particle. The conduction parameter κ can range from 0 to 6×10^{-7}, the full Spitzer value for a plasma (Spitzer 1962). If κ is zero, one has a first order linear equation for $T(r)$.

In a plasma with a smooth density distribution, the gas density can be directly related to the count rate emissivity

$$C(r) = n^2\, V(T), \quad (10)$$

where the function $V(T)$ is the gas emissivity folded through the detector response function —

$$V(T) = \frac{1}{4\pi D^2}\int \frac{\epsilon(E,T)}{E} A(E)\, e^{-N_H \sigma_H(E)}\, dE. \quad (11)$$

the emissivity of the gas as a function of energy and temperature, $A(E)$ is the effective area of the detector as a function of energy, N_H is the hydrogen column density of gas along the line of sight through our own galaxy, and σ_H is the cross section per hydrogen atom as a function of energy.

C(r) is determined by our fits of the double King models to the X-ray surface brightness profiles. We can now substitute for the density n in equation (4) to obtain a differential equation for the temperature distribution that consists entirely of known and observable quantities and the single parameter $\dot{M}$ —

$$\begin{aligned}\frac{\partial}{\partial r}\left[r^2\kappa T^{5/2}\frac{\partial T}{\partial r}\right] &= -r^2\frac{C(r)}{V(T)}\Lambda(T) \\ &\quad - \dot{M}k4\pi\mu m_H\left[\left(\frac{1}{\gamma-1} + \frac{1}{2}\frac{\partial ln\, V}{\partial ln\, T}\right)\frac{\partial T}{\partial r} - \frac{1}{2}\frac{T}{r}\frac{\partial ln\, C}{\partial ln\, r}\right]. \quad (12)\end{aligned}$$

The parameter $\dot{M}$ and the resulting temperature profile is constrained by the spectral information available from the spatially resolved projected temperatures obtained in §3. Given $T(r)$ and $n(r)$, one can solve equation (2) directly for the potential.

7. Conclusions

We observed three poor clusters with central dominant galaxies (AWM 4, MKW 4, and MKW 3s) using the Position Sensitive Proportional Counter on the ROSAT X-ray satellite. The images reveal smooth, symmetrical X-ray emission filling the cluster with a sharp peak on each central galaxy. The cluster surface brightness profiles can be decomposed using superposed King models for the central galaxy and the intracluster medium. The King model parameters for the cluster portions are consistent with previous observations of these clusters. The newly measured King model parameters for the central galaxies are typical of the X-ray surface brightness distributions of isolated elliptical galaxies.

Spatially resolved temperature measurements in annular rings throughout the clusters show a nearly isothermal profile. Temperatures are consistent with previously measured values, but are much better determined. Calculated cooling times provide evidence for the presence of cooling flows in all clusters observed, but there is no significant drop in temperature noted in the innermost bins where cooling flows are likely to be present, nor is any excess absorption by cold gas required. All cold gas columns are consistent with galactic foreground absorption.

We derived mass profiles for the clusters assuming both isothermal temperature profiles and cooling flow models with constant mass flow rates. There is little difference between the mass profiles from the cooling flow fits and the assumed isothermal models except in the central-most regions where the instrumental resolution comes into play. Our results are consistent with previous Einstein IPC observations by Kriss, Cioffi, & Canizares, but extend the mass profiles out to 1 Mpc in these poor clusters. Cluster masses slightly exceed 10^{14} solar masses for AWM 4 and MKW 3s. The ratio of gas mass to binding mass rises with radius, but at 1 Mpc it is only 5–25% of the binding mass.

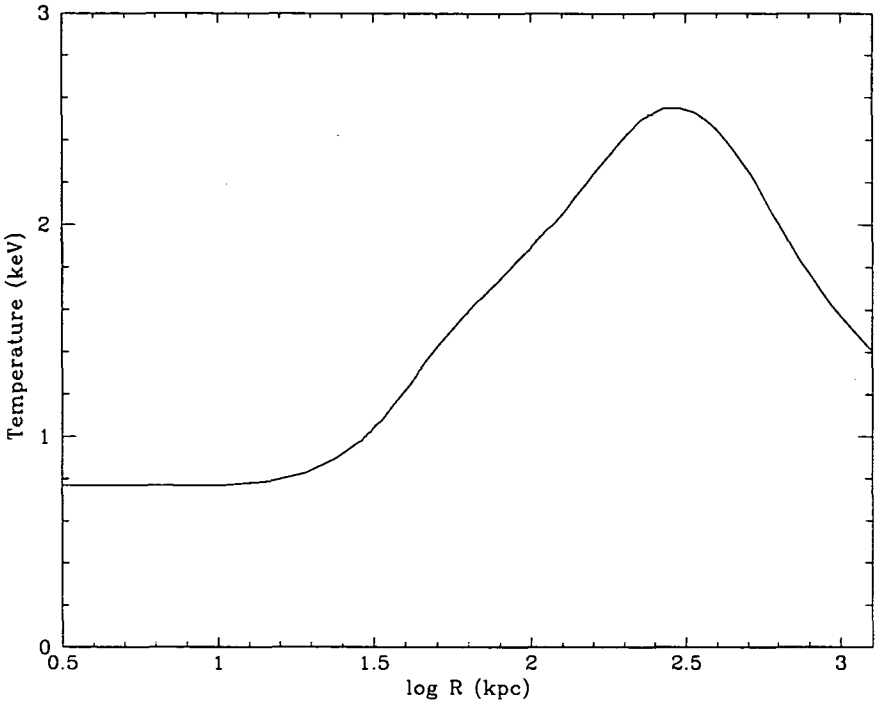

Fig. 19.— Temperature vs. radius in AWM 4 for a cooling flow model with a constant mass flow rate that matches the X-ray surface brightness profile and the spectral data.

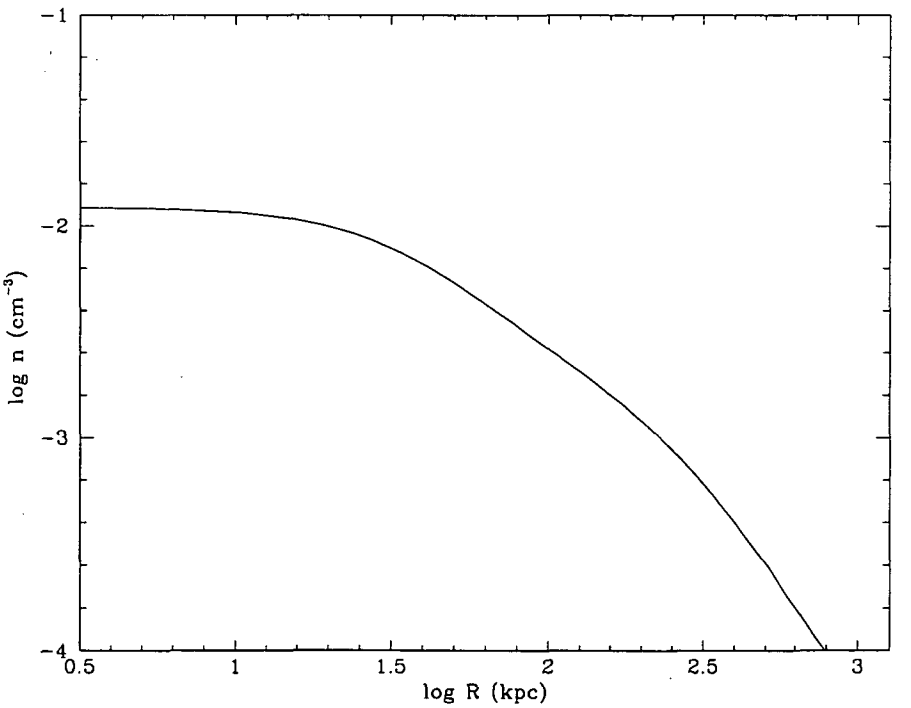

Fig. 20.— Gas density vs. radius in AWM 4 for a cooling flow model with a constant mass flow rate that matches the X-ray surface brightness profile and the spectral data.

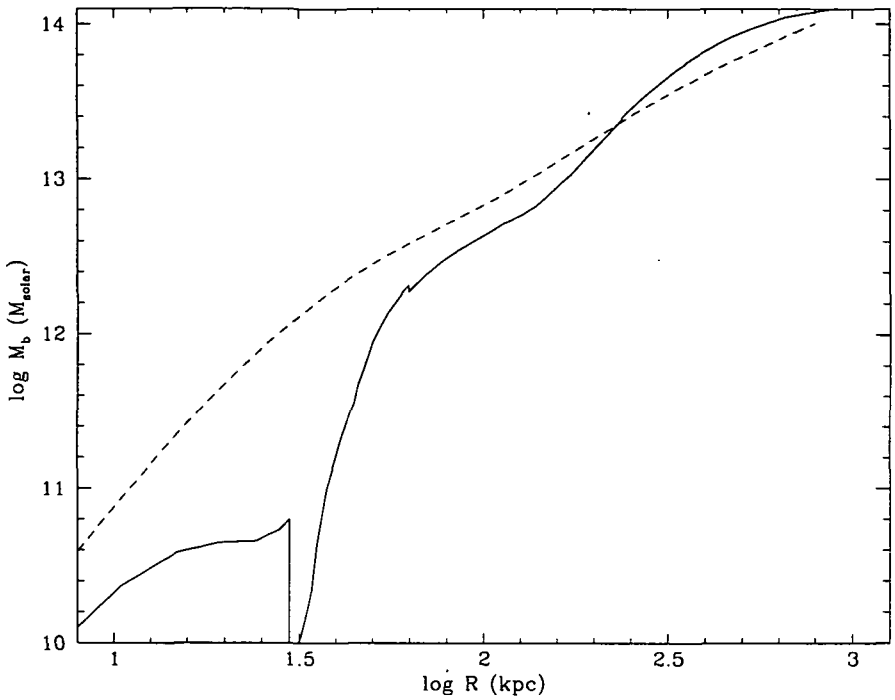

Fig. 21.— The figure shows the cumulative binding mass vs. radius (solid line) obtained from the cooling flow model fit to AWM 4. For comparison, the binding mass derived earlier assuming isothermal gas and hydrostatic equilibrium is shown as a dotted line.

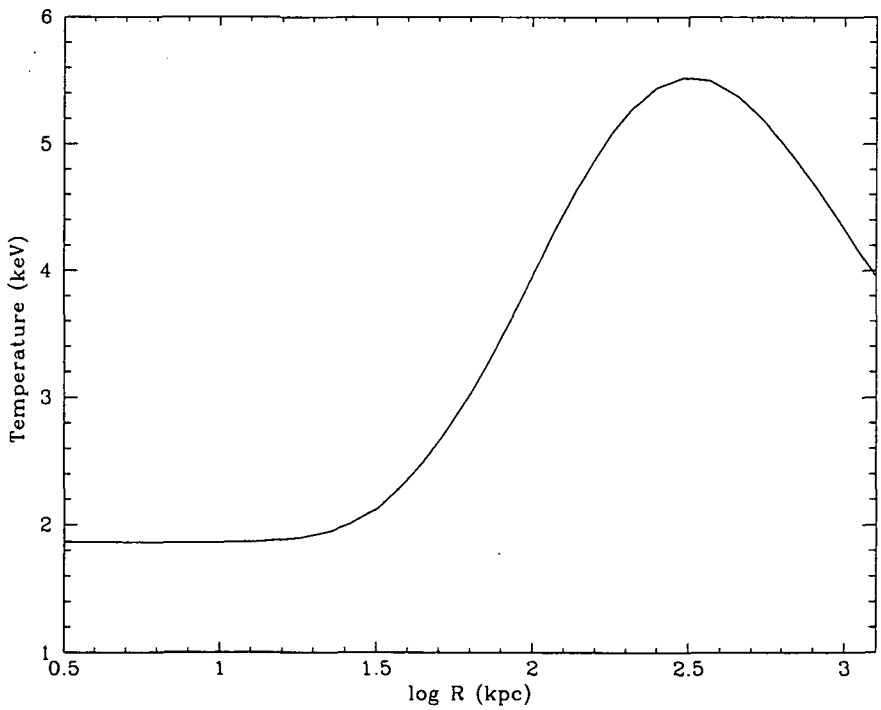

Fig. 22.— Temperature vs. radius in MKW 3s for a cooling flow model with a constant mass flow rate that matches the X-ray surface brightness profile and the spectral data.

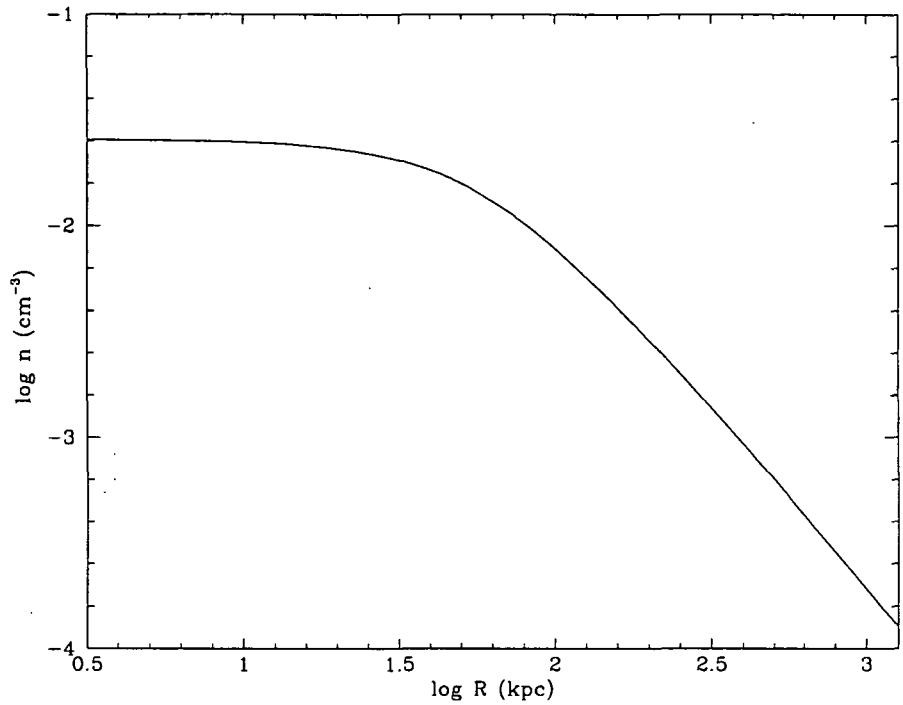

Fig. 23.— Gas density vs. radius in MKW 3s for a cooling flow model with a constant mass flow rate that matches the X-ray surface brightness profile and the spectral data.

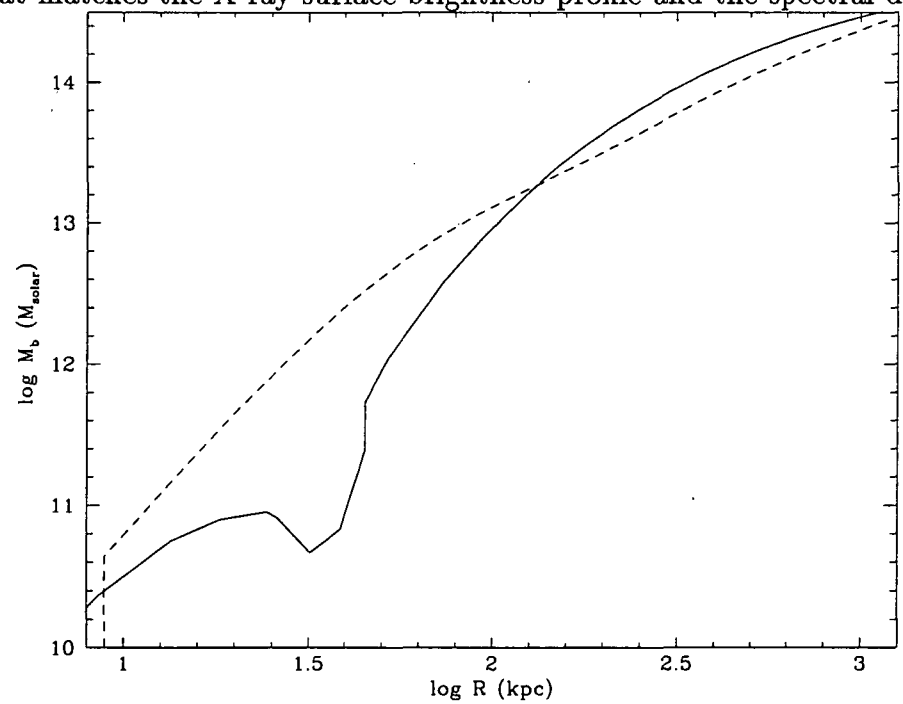

Fig. 24.— The figure shows the cumulative binding mass vs. radius (solid line) obtained from the cooling flow model fit to MKW 3s. For comparison, the binding mass derived earlier assuming isothermal gas and hydrostatic equilibrium is shown as a dotted line.

References

Albert, C. E., R. A. White, & W. W. Morgan, 1977, *Astrophys. J.*, **211**, 309.

Bahcall, N. A. 1980, ApJ, 238, L117.

Bahcall, N. A., 1981, *Astrophys. J.*, **247**, 787.

Beers, T. C., Geller, M. J., Huchra, J. P., Latham, D. W., and Davis, R. J. 1984, ApJ, 283, 33.

Canizares, C. R., Stewart, G. C., & Fabian, A. C. 1983, ApJ, 272, 449.

Cowie, L. L., Henriksen, M. J., and Mushotzky, R. 1987, ApJ, 317, 593.

Fabian, A. Hu, E. M., Cowie, L. L., and Grindlay, J. 1981, ApJ, 248, 47.

Fabian, A. C., P. E. J. Nulsen, & C. R. Canizares, 1991, *Astronomy and Astrophysics Review*, **2**, 191.

Fabian, A. C., P. E. Nulsen, & C. R. Canizares, 1984, Nature, 310, 733

Fabricant, D., G. Rybicki, & P. Gorenstein, 1984, *Astrophys. J.*, **286**, 186.

Forman, W., C. Jones, & W. Tucker, 1985, *Astrophys. J.*, **293**, 102.

Hausman, M. A., and Ostriker, J. P. 1978, ApJ, 224, 320.

Hill, J. M. et al. 1988, ApJ, 332, L23.

Jones, C., and W. Forman, 1984, *Astrophys. J.*, **276**, 38.

King, I. R., 1962, *Astron. J.*, **67**, 471.

Kriss, G. A., Canizares, C. R., McClintock, J. E., & Feigelson, E. D. 1980, ApJ, 235, L61.

Kriss, G. A., D. F. Cioffi, & C. R. Canizares, 1983, *Astrophys. J.*, **272**, 439.

Malumuth, E. M., & R. P. Kirshner, 1981, *Astrophys. J.*, **251**, 508.

Malumuth, E. M., & Kirshner, R. P. 1985, ApJ, 291, 8.

Malumuth, E. M., & G. A. Kriss, 1986, *Astrophys. J.*, **308**, 10.

Malumuth, E. M., Kriss, G. A., Ferguson, H. C., Dixon, W. V. D., & Ritchie, C. 1992, AJ, 104, 495.

Merritt, D. 1983, ApJ, 264, 24.

Merritt, D. 1984, ApJ, 276, 26.

Morgan, W. W., S. Kayser, & R. A. White, 1975, *Astrophys. J.*, **199**, 545.

Morrison, J., & McCammon, R., 1983, *Astrophys. J.*, **270**, 119.

Plucinsky, P. L., S. L. Snowden, U. G. Briel, G. Hasinger, & E. Pfeffermann, 1993, *Astrophys. J.*, **418**, 519.

Raymond, J. C., D. P. Cox, & B. W. Smith, 1976, *Astrophys. J.*, **204**, 290.

Raymond, J. C., & B. W. Smith, 1977, *Astrophys. J. Suppl.*, **35**, 419.

Richstone, D. O., & Malumuth, E. M. 1983, ApJ, 268, 30.

Schneider, D. P., Gunn, J. E., and Hoessel, J. G. 1983, ApJ, 264, 337.

Sharples, R. M., Ellis, R. E., and Gray, P. M. 1988, MNRAS, 231, 479.

Snowden, S. L., & M. J. Freyberg, 1993, *Astrophys. J.*, **404**, 403.

Snowden, S. L., D. McCammon, D.N. Burrows, & J. A. Mendenhall, 1994, *Astrophys. J.*, **424**, 714.

Snowden, S. L., P. P. Plucinsky, U. Briel, G. Hasinger, & E. Pfefferman, 1992, *Astrophys. J.*, **393**, 819.

Spitzer, L. 1962, Physics of Fully Ionized Gases, (New York: Wiley-Interscience).

Stark, A. A., C. F. Gammie, R. W. Wilson, J. Bally, R. A. Linke, C. Heiles, & M. Hurwitz, *Astrophys. J. Suppl.*, **79**, 77.

Stewart, G. C., A. C. Fabian, C. Jones, & W. Forman, 1985, *Astrophys. J.*, **285**, 1.

Thuan, T. X., & W. Romanishin, 1981, *Astrophys. J.*, **248**. 439.

Trincheri, G., G. Fabbiano, & G. R. Canizares, 1985, *Astrophys. J.*, **310**, 637.

White, D. A., Fabian, A. C., Johnstone, R. M., Mushotzky, R. F., & Arnaud, K. A. 1991, *Monthly Notices of the Royal Astronomical Society*, **252**, 72.